

Phase control of the Autler-Townes doublet in multistate systemsT. Bayer, K. Eickhoff , D. Köhnke , and M. Wollenhaupt **Institut für Physik, Carl von Ossietzky Universität Oldenburg, Carl-von-Ossietzky-Straße 9-11, D-26129 Oldenburg, Germany*

(Received 6 July 2023; accepted 8 September 2023; published 22 September 2023)

The resonant dynamic Stark effect, observed in the Autler-Townes (AT) splitting, plays a central role in ultrafast strong-field physics. Recent experiments have demonstrated the phase control of the AT doublet in atomic resonance-enhanced multiphoton ionization using intense resonant shaped femtosecond laser pulses [Bayer *et al.*, *Adv. Chem. Phys.* **159**, 235 (2016)]. Based on a two-state model, we showed that the underlying control mechanism is the selective population of dressed states (SPODS). In this work, we use a numerical model to calculate the photoelectron momentum distribution (PMD) based on the *ab initio* solution of the two-dimensional (2D) time-dependent Schrödinger equation (TDSE) to obtain a more complete physical picture of the nonperturbative control of the AT doublet. The 2D-TDSE model reproduces the ultrafast switching among the AT components while also revealing deviations from the signatures predicted by the two-state model. These deviations are attributed to the influence of additional intermediate states. To rationalize our observations, we propose a refined five-state model that includes all significantly populated bound states from the full calculation and accurately reproduces the 2D PMD. Based on the validated five-state model, we conduct a dressed-state analysis which provides a clear physical picture of the SPODS mechanism in a multistate system and sheds light on the role of the intermediate states in strong-field control.

DOI: [10.1103/PhysRevA.108.033111](https://doi.org/10.1103/PhysRevA.108.033111)**I. INTRODUCTION**

In strong-field coherent control, nonperturbative quantum dynamics are manipulated by intense shaped laser pulses to efficiently guide a quantum system from its initial state into a preselected target state [1–3]. Due to the dynamic Stark effect, nonperturbative interactions are generally accompanied by modifications of the potential-energy landscape [4–9]. In the presence of resonances, the dynamic Stark effect is observed in the Autler-Townes (AT) splitting. The AT effect [10] arises when two quantum states are strongly coupled by a resonant electromagnetic field and probed by a weak transition to a third state acting as a spectator. If the driving field is sufficiently intense to induce Rabi oscillations between the first two states, the probe transition to the third state splits into two components energetically separated by the corresponding Rabi frequency. Originally discovered in the microwave regime [10], the AT effect was soon transferred to the optical regime [5,11,12]. Today, the AT effect is a cornerstone of many areas of physics comprising high-resolution spectroscopy [13–15], electromagnetically induced transparency [16,17], laser cooling of atoms [18], and quantum information processing [19–21].

Meanwhile, coherent Rabi-type dynamics and the formation of the AT doublet have been demonstrated in the extreme-ultraviolet (XUV) regime in experimental studies on the resonance-enhanced multiphoton ionization (REMPI) of helium atoms using femtosecond pulses from a free-electron laser [22]. Furthermore, the ultrafast buildup of the AT doublet in strongly driven noble-gas atoms has been observed in real

time using XUV attosecond transient absorption spectroscopy [23–26].

Recently, we demonstrated phase control of the AT doublet in the (1 + 2) REMPI of potassium atoms by intense shaped femtosecond laser pulses [5]. The control mechanism was shown to be the selective population of dressed states (SPODS) [3,27–29], realized by adjusting the optical phase of the driving field to the phase of the field-induced charge dynamics. A recent review of SPODS can be found in [30]. Besides the dressed-atom approach, the SPODS mechanism was discussed in various physical pictures, including the bare-state description [5], the Bloch vector model [28,29], and the laser-induced electric dipole dynamics [8,31]. The different pictures were derived from a numerical model based on solving the time-dependent Schrödinger equation (TDSE) for the bound atomic system in a multistate basis [30,32,33] and calculating the energy-resolved photoelectron spectrum using time-dependent perturbation theory [5,34]. In general, level-based models are powerful tools to elucidate the essential physics underlying complex light-induced quantum dynamics. Identifying all pivotal states involved in the interaction, however, can be difficult, especially in the case of multiphoton excitations.

In this paper, we use an *ab initio* ansatz to study the AT control scheme via SPODS. In addition, we analyze the energy- and angle-resolved photoelectron spectrum, i.e., the photoelectron momentum distribution (PMD), which provides detailed information on the ionization dynamics [35,36]. One of the key advantages of *ab initio* models is their inherent incorporation of all intermediate resonances and interstate couplings. The availability of the wave function along with the knowledge of its time evolution provides full access to all observables and their time dependence. Recently, we

*Corresponding author: matthias.wollenhaupt@uol.de

developed a numerical model based on the *ab initio* solution of the two-dimensional (2D) TDSE to investigate the interaction of quantum systems with ultrashort polarization-shaped laser pulses and the calculation of the 2D PMD [37]. We validated the accuracy and reliability of our 2D-TDSE model by reproducing recent experimental [37–39] and theoretical [40] results on free-electron vortices created by atomic multiphoton ionization (MPI). Subsequently, we applied the model to investigate molecular free-electron vortices [41] previously investigated in [42]. Here, we apply this model to obtain a more complete physical picture of the nonperturbative dynamics underlying the phase control of the AT doublet in $(1 + 2)$ REMPI of potassium using phase-locked double pulses [5,27]. Our results show that the model reproduces the ultrafast and efficient switching between the AT components via the relative phase, which is characteristic of SPODS implemented by pulse sequences [3,5,28,30,31,43]. However, we also find distinct deviations between the *ab initio* results and the predictions of a simple two-state model. Besides the 2D PMD itself, which exhibits richer structures in the 2D-TDSE simulation than in the two-state model, we encounter deviations from the SPODS signatures derived in our previous work [30], particularly in the analysis of relevant observables such as the bound-state population dynamics, the induced dipole dynamics, and the time-dependent interaction energy. These deviations are attributed to the influence of high-lying intermediate states in the $(1 + 2)$ REMPI pathways. To rationalize our observations, we devise a five-state model including all relevant bound states populated in the *ab initio* calculation. The refined five-state model is validated against the 2D-TDSE model [44,45] by reproducing the bound-state population dynamics and the 2D PMD. Finally, the dressed-state analysis of the five-state model provides a transparent physical picture of the AT control mechanism in the full calculation and reveals the importance of intermediate states in strong-field control.

II. 2D-TDSE MODEL

A. Theoretical description and numerical details

The numerical methods used in our 2D-TDSE model were described in detail elsewhere [37,46]. Briefly, we solve the 2D-TDSE in the dipole approximation and length gauge

$$i\hbar \frac{\partial}{\partial t} \psi(\mathbf{r}, t) = \left[-\frac{\hbar^2}{2m_e} \Delta + V(r) + e\mathbf{r} \cdot \mathbf{E}(t) \right] \psi(\mathbf{r}, t) \quad (1)$$

($\mathbf{r} = x\mathbf{e}_x + y\mathbf{e}_y$) for a single active electron with mass m_e and charge $-e$ in the soft-core Coulomb potential [47–49]

$$V(r) = -\frac{ze^2}{4\pi\epsilon_0} \frac{\text{erf}(r/a)}{r}, \quad (2)$$

interacting with an, in general, polarization-shaped laser electric field $\mathbf{E}(t)$. The eigenfunctions $\psi_n(\mathbf{r})$ and eigenenergies ϵ_n of the potential are obtained by solving the time-independent Schrödinger equation using the Fourier grid Hamiltonian method [50]. To mimic the experimental conditions [30], we reproduce the ground-state energy $\epsilon_{1s} = -4.34$ eV and the first-excited-state energy $\epsilon_{2p} = -2.73$ eV of the potassium atom [51] by choosing an effective nuclear charge of $z = 0.9085$ and a soft-core parameter of $a = 2.3065$ Å in Eq. (2).

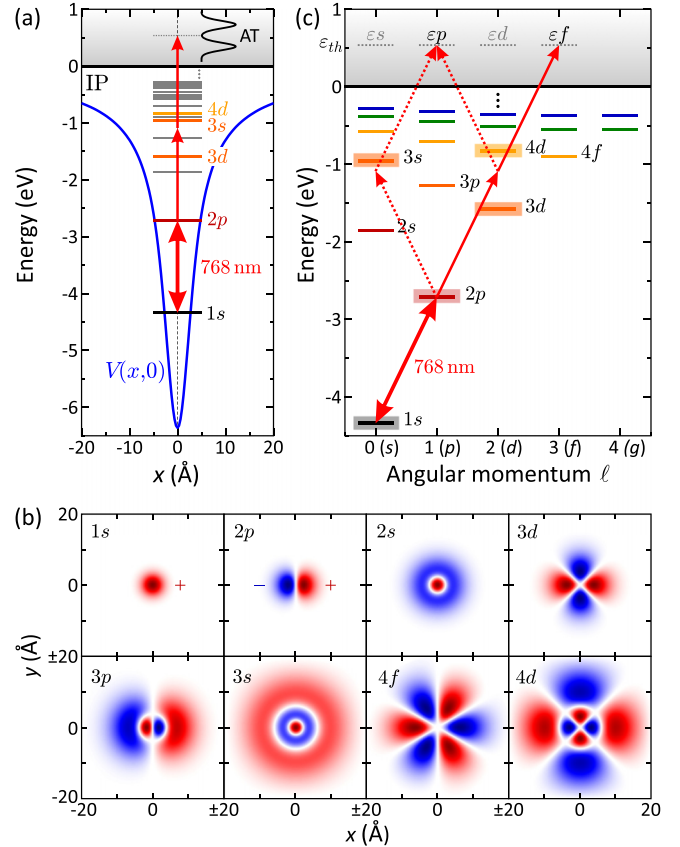


FIG. 1. Physical system. (a) Section through the 2D soft-core Coulomb potential from Eq. (2) along the x axis. The horizontal lines indicate the electronic eigenenergy levels. (b) Real-valued atomic wave functions of the lowest eight eigenstates. The labels are adopted from the 3D hydrogen atom. All states except for the s states are twofold degenerate (the respective orthogonal orbitals are not shown). (c) Grotrian diagram and excitation scheme for the $(1 + 2)$ REMPI of the potassium atom by a 768-nm field (red arrows) creating photoelectron wave packets with kinetic energies centered around $\epsilon_{\text{th}} = 0.5$ eV.

The labeling of states, however, is adopted from the hydrogen atom. The reason for this choice of notation is that the corresponding orbitals (see Fig. 1 and discussion in Sec. II B) are consistent with hydrogen rather than potassium since the atom is modeled as a one-electron system. The energy difference between ground and first excited states corresponds to a transition wavelength of $\lambda_{1s \rightarrow 2p} = 768$ nm [see Fig. 1(a)]. The laser field $\mathbf{E}(t)$ used in this contribution is linearly polarized in the y direction and tuned to the $1s \rightarrow 2p$ resonance by setting its central frequency to $\omega_0 = 2\pi c/\lambda_{1s \rightarrow 2p} = 2.45$ rad/fs. The field is described by its positive-frequency analytic signal, consisting of two subpulses

$$\mathcal{E}^+(t) = \mathcal{E}_1 e^{i\varphi_1} g(t - \tau_1) + \mathcal{E}_2 e^{i\varphi_2} g(t - \tau_2) \quad (3)$$

with individual amplitudes \mathcal{E}_n , phases φ_n , and time delays τ_n ($n = 1, 2$). The temporal envelope function $g(t)$ is Gaussian shaped with unit amplitude and a duration of $\Delta t = 15$ fs (full width at half maximum of the intensity). The vectorial field is given by the real part of Eq. (3) as $\mathbf{E}(t) = \Re[\mathcal{E}^+(t)e^{i\omega_0 t}] \mathbf{e}_y$.

Initially, the atom is prepared in the $1s$ ground state. The initial wave function $\psi_{1s}(\mathbf{r})$ is refined by imaginary-time propagation [52]. Subsequently, the wave function $\psi(\mathbf{r}, t)$ is propagated on a discrete spatial grid with boundaries at $(x_{\max}, y_{\max}) = -(x_{\min}, y_{\min}) = (500 \text{ \AA}, 500 \text{ \AA})$ using a Fourier-based split-operator technique [53]. The spatial and temporal step sizes are $\delta x = \delta y = 1 \text{ \AA}$ and $\delta t = 10 \text{ as}$, respectively. Nonphysical reflections at the spatial boundaries are minimized using absorbing boundary conditions [54,55]. After the interaction with the laser pulse, the wave function is propagated until the free part $\psi_f(\mathbf{r}, t)$, i.e., the photoelectron wave packet, has detached from the bound part but not yet reached the absorbing boundaries. At this time, $t = t_f$, the photoelectron wave function is separated from the bound part by application of a circular splitting filter [56]. Fourier transformation of the free part yields the 2D PMD

$$\mathcal{P}(\mathbf{k}) = |\mathcal{F}[\psi_f(\mathbf{r}, t_f)](\mathbf{k})|^2. \quad (4)$$

Numerically, we can track the continuous transformation of the coordinate-space density into the PMD [37,57] in time by propagating the wave function even further than t_f on an extended grid. We illustrate this process in Sec. III A, where we discuss the formation dynamics of the AT doublet in the 2D PMD.

The PMD $\mathcal{P}(\mathbf{k}) = \mathcal{P}(k, \phi)$ is mostly discussed in energy representation $\mathcal{P}(\varepsilon, \phi)$, with $\varepsilon(k) = (\hbar k)^2/2m_e$ being the photoelectron kinetic energy, and then referred to as PED. In addition to the 2D PMD (or PED) and the time-dependent coordinate-space density $\varrho(\mathbf{r}, t) = |\psi(\mathbf{r}, t)|^2$, we consider various observables \mathcal{O} to gain insights into the physical mechanisms behind the nonperturbative ionization dynamics. For this purpose, we analyze the time evolution of the corresponding expectation values $\langle \mathcal{O} \rangle(t) = \langle \psi(t) | \mathcal{O} | \psi(t) \rangle$. The time-dependent bound-state population dynamics is obtained by calculating the expectation value of the projection operator $p_n = |\psi_n\rangle\langle\psi_n|$ as

$$\langle p_n \rangle(t) = \langle \psi(t) | \psi_n \rangle \langle \psi_n | \psi(t) \rangle = \left| \iint_{-\infty}^{+\infty} \psi_n^*(\mathbf{r}) \psi(\mathbf{r}, t) d^2r \right|^2. \quad (5)$$

The two observables which are closely related to the dressed states of the interacting laser-atom system are the field-induced charge oscillation and the total interaction energy [30]. The former is captured by the expectation value of the dipole operator $\boldsymbol{\mu} = -e\mathbf{r}$ and calculated as

$$\langle \boldsymbol{\mu} \rangle(t) = \langle \psi(t) | \boldsymbol{\mu} | \psi(t) \rangle = -e \iint_{-\infty}^{+\infty} \mathbf{r} \varrho(\mathbf{r}, t) d^2r. \quad (6)$$

The latter is given by the expectation value of the time-dependent Hamiltonian $\mathcal{H}(t)$ on the right-hand side of the TDSE in Eq. (1),

$$\begin{aligned} \langle \mathcal{H} \rangle(t) &= \langle \psi(t) | \mathcal{H}(t) | \psi(t) \rangle \\ &= \langle \psi(t) | [\mathcal{H}_0 - \boldsymbol{\mu} \cdot \mathbf{E}(t)] | \psi(t) \rangle \\ &= \sum_n \langle p_n \rangle(t) \varepsilon_n - \langle \boldsymbol{\mu} \rangle(t) \cdot \mathbf{E}(t). \end{aligned} \quad (7)$$

In the last step, we have expanded the wave function in the eigenbasis $\{|\psi_n\rangle\}$ of the unperturbed Hamiltonian \mathcal{H}_0 with

TABLE I. Spectroscopic characterization of the transitions between the lowest eight eigenstates, $1s$ to $4d$ [see Fig. 1(b)]. The lower triangle contains the numerically calculated transition dipole matrix elements $\mu_{nm} = |\langle \psi_n | \boldsymbol{\mu} | \psi_m \rangle|$ in units of (ea_0) . The upper triangle contains the corresponding transition wavelengths $\lambda_{nm} = hc/(\varepsilon_n - \varepsilon_m)$ in nanometers for transitions with nonzero dipole coupling.

	$1s$	$2p$	$2s$	$3d$	$3p$	$3s$	$4f$	$4d$
$1s$		768			402			
$2p$	2.86					700		656
$2s$	0	3.80			2049			
$3d$	0	3.31	0		3748		1821	
$3p$	0.295	0	6.24	4.06		4122		2953
$3s$	0	0.486	0	0	8.68			
$4f$	0	0	0	4.98	0	0		17763
$4d$	0	0.577	0	0	6.20	0	6.66	

corresponding eigenenergies ε_n . The first term in Eq. (7) describes the mean excitation energy $\langle \varepsilon_{\text{exc}} \rangle(t) = \sum_n \langle p_n \rangle(t) \varepsilon_n$ transferred from the field to the atom at time t . The second term $\langle \varepsilon_{\text{int}} \rangle(t) = -\langle \boldsymbol{\mu} \rangle(t) \cdot \mathbf{E}(t)$ describes the energy of the induced electric dipole in the external field, which is closely related to the energies of the dressed states. In the two-state model, the maximization (minimization) of $\langle \varepsilon_{\text{int}} \rangle(t)$ corresponds to the selective population of the upper (lower) dressed state and vice versa [8,30,31]. We show in Sec. III B that this relation is not always valid in a more realistic multistate system.

B. Characterization of the physical system

The spectroscopic characterization of the atomic system is relevant both for the design of the control scenarios and for the analysis of the results. Moreover, information on the electronic structure of the system is required to set up a level-based model system consistent with the 2D-TDSE model. Figure 1(a) shows a section $V(x, y = 0)$ through the 2D potential from Eq. (2) along the x axis, together with the bound-state energy levels ε_n obtained by solving the 2D-TDSE (see Sec. II A). The ground and first excited states are resonantly coupled by a laser pulse with central wavelength $\lambda_0 = 768 \text{ nm}$. In $(1+2)$ REMPI, the simultaneous absorption of two additional photons maps the excited-state dynamics to the photoionization continuum, giving rise to the AT doublet in the photoelectron energy spectrum (black line). The eigenfunctions $\psi_n(\mathbf{r})$, i.e., orbitals of the lowest eight energy levels are depicted in Fig. 1(b). They are real valued, with signs encoded by the color (red for negative, blue for positive). By inspection of the nodal structure, each orbital is assigned a principal quantum number n and an orbital angular momentum quantum number ℓ . Except for the s states, all eigenstates are twofold degenerate. The respective orthogonal orbitals are not shown. Based on the quantum number assignment, we plot a Grotrian diagram in Fig. 1(c). The main excitation and ionization pathways are identified by calculation of the transition dipole moments $\boldsymbol{\mu}_{nm} = \langle \psi_n | \boldsymbol{\mu} | \psi_m \rangle$. The absolute values $\mu_{nm} = |\boldsymbol{\mu}_{nm}|$ of the couplings between the eight lowest energy states are listed in the lower triangle of Table I in units of ea_0 . The corresponding transition wavelengths

$\lambda_{nm} = hc/(\varepsilon_n - \varepsilon_m)$ in nanometers are listed in the upper triangle. The numerical results reproduce the selection rule $\Delta\ell = \pm 1$. Accordingly, in Fig. 1(c), the (1 + 2) REMPI process branches at the $2p$ state into the three different ionization pathways [58] indicated by red arrows. The first pathway, $1s \rightarrow 2p \rightarrow nd \rightarrow \varepsilon f$, proceeds via d -type intermediate states, leading to an f -type continuum. The second pathway, $1s \rightarrow 2p \rightarrow nd \rightarrow \varepsilon p$, branches off at the d intermediates to end up in a p -type continuum. The same continuum is accessed by the third pathway, $1s \rightarrow 2p \rightarrow ns \rightarrow \varepsilon p$, via s -type intermediates. The intermediate states which we identified to play key roles in the ionization dynamics are highlighted in Fig. 1(c). Besides the resonantly coupled states $1s$ and $2p$, these are states $3d$, $3s$, and $4d$, which are nearly resonant at the two-photon level.

III. RESULTS

The results are presented in two parts. First, we investigate the formation dynamics of the AT doublet by tracking the time evolution of the coordinate-space wave function (Sec. III A). Second, we discuss the phase control of the AT doublet via SPODS by double-pulse sequences (Sec. III B), as demonstrated experimentally in [5,27].

A. Formation dynamics of the AT doublet

The formation of the AT doublet in the photoelectron energy spectrum can be understood analogously to the formation of the discrete series of peaks generally attributed to above-threshold ionization (ATI) [59]. In a spatiotemporal picture, the ATI series is generated by the interference of ultrashort electron bursts released every cycle of the laser pulse when the electric-field amplitude reaches a maximum (in a specific direction). Since these bursts occur with a period of $2\pi/\omega_0$, the ultrabroad spectrum of each photoelectron pulse is modulated periodically with a period of $\hbar\omega_0$, giving rise to the series of ATI peaks separated by the mean photon energy [60]. Analogously, the formation of the AT doublet is explained by replacing the optical-field oscillation with the Rabi oscillation. Whenever the excited-state population (here $2p$) reaches a maximum, the ionization probability is likewise enhanced, and a short electron burst is released. These bursts occur with a period of $2\pi/\Omega_0$ if Ω_0 denotes the Rabi frequency and if we assume a flat-top laser pulse for the sake of the argument. The interference of these electron pulses induces a splitting of *each* ATI peak into two components separated by $\hbar\Omega_0$: the AT doublet.

Our simulation allows us to track the formation dynamics of both the ATI contributions and the AT doublet directly in the coordinate-space wave function of the outgoing photoelectron. To this end, we excite the atom with a single resonant laser pulse by setting $\mathcal{E}_1 = 0$, $\mathcal{E}_2 = 3.6 \times 10^7$ V/cm, $\varphi_2 = 0$, and $\tau_2 = 0$ in Eq. (3). The numerical results are presented in Fig. 2. The laser field is depicted in the top frame of Fig. 2(a). The field amplitude \mathcal{E}_2 corresponds to a pulse area [33] of

$$\theta_\infty = \frac{\mu_{2p,1s} \mathcal{E}_2}{\hbar} \int_{-\infty}^{\infty} g(t) dt = 6\pi, \quad (8)$$

with respect to the resonant transition $1s \rightarrow 2p$. The induced population dynamics $\langle p_n \rangle(t)$ derived from the wave function

$\psi(\mathbf{r}, t)$ is shown in the bottom frame. In accordance with the pulse area of 6π , the populations of the ground state $1s$ and resonant state $2p$ (thick black and red lines) undergo three Rabi cycles, albeit with decreasing amplitude. The fast oscillations superimposed on the population dynamics with a frequency of $2\omega_0$ are induced by the antiresonant component of the field. The damping of the Rabi oscillation is due to the coupling of the resonant $1s$ - $2p$ subsystem to higher-lying intermediate states. In particular, states $3s$ (green line) and $4d$ (blue line) are populated efficiently during the interaction and are finally populated by 10% and 25%, respectively. In addition, the $3d$ state (yellow line) is populated transiently by up to 20%. All other states are excited only insignificantly. Their accumulated population is plotted as a gray line. This result shows that resonant states $1s$ and $2p$ together with intermediate states $3d$, $3s$, and $4d$ play key roles in the interaction. Therefore, these five states are included in our tailored multistate model. The $3p$ state, despite its strong coupling to states $3s$ and $3d$ (see Table I), is not included because the corresponding transitions are far detuned from resonance with the 768-nm pulse, preventing the efficient excitation of this state. Figure 2(b) shows the energy-resolved PMD, i.e., the PED $\mathcal{P}(\varepsilon, \phi)$, at $t = \infty$ in a logarithmic representation. The spectrum shows a prominent threshold contribution centered around $\varepsilon_{\text{th}} = 0.5$ eV. In addition, we observe two ATI contributions around $\varepsilon_{\text{th}} + \hbar\omega_0 = 2.1$ eV and $\varepsilon_{\text{th}} + 2\hbar\omega_0 = 3.7$ eV. Each contribution exhibits an AT splitting of $\hbar\Omega_0 = 460$ meV.

To study the formation dynamics of the AT doublet primarily in the threshold contribution, we examine the time evolution of the coordinate-space wave function $\psi(\mathbf{r}, t)$ and focus on the created photoelectron wave packet $\psi_f(\mathbf{r}, t)$. Figure 2(c) shows a series of snapshots of the electron density $\varrho(\mathbf{r}, t)$ at distinct times during [frames (i)–(iii)] and after [frames (iv)–(vii)] the interaction. Every time the $2p$ -population oscillation reaches a maximum [colored arrows in Fig. 2(a) labeled by (i), (ii), and (iii)], a photoelectron partial wave packet is released. In total, we hence observe three distinct photoelectron bursts; the first one, which is around $t = -8.8$ fs, is marked by a red arrow in frame (i), the second one, around $t = 0.9$ fs, is marked by a green arrow in frame (ii), and the third one, around $t = 11.7$ fs, is marked by a blue arrow in frame (iii). After the interaction, the photoelectron wave function evolves field free under the influence of the weak, but long-range, Coulomb-type potential. As the three partial wave packets propagate outwards, they spread and disperse into a single wave packet. In the intermediate propagation regime between $t = 30$ and 75 fs [frames (iv)–(vi)], their interference gives rise to complicated radial fringe patterns. These patterns are easily discernible in the angle-integrated representation of the density displayed on top of the 2D plots in Fig. 2(c). The insets magnify a weak, but fast, contribution propagating ahead of the main wave packet (violet arrow), indicating the formation of the first ATI. Asymptotically, the radial fringe pattern resolves into a regularly shaped double-hump distribution [frame (vii)], i.e., the AT spectrum and its replica in the ATI. The convergence occurs roughly within 120 fs after the interaction. Subsequently, the wave packet expands without substantially altering its shape. The asymptotic shape matches the shape of the calculated PMD [37,57]. For comparison, the angularly

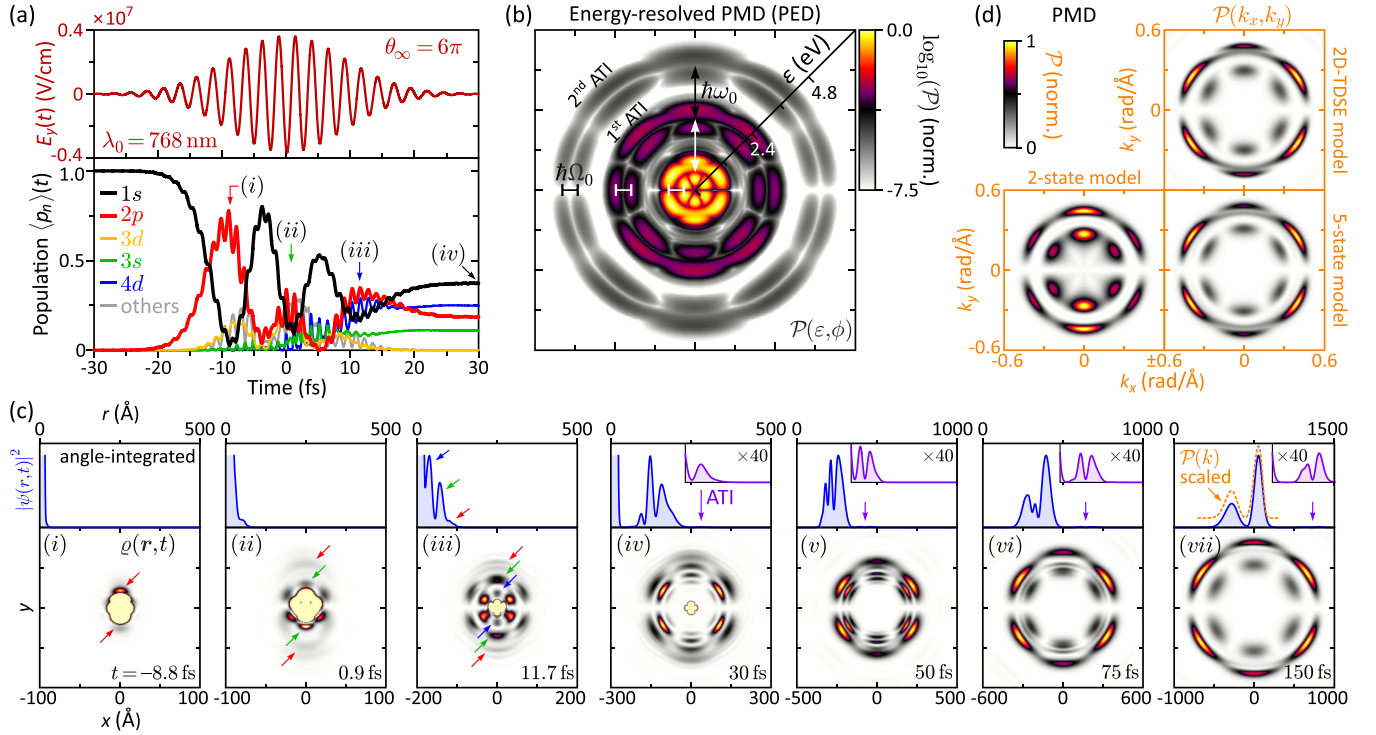


FIG. 2. Temporal formation dynamics of the AT doublet in the photoelectron wave function created by a single intense resonant laser pulse. The pulse is depicted in (a) on top of the induced bound-state population dynamics, showing Rabi cycling between the ground state $1s$ and the resonant excited state $2p$. (b) Created PED in logarithmic representation to display the threshold contribution as well as the first and second ATIs, each of which exhibits an AT splitting of $\hbar\Omega_0 = 480$ eV. (c) Time series of the photoelectron density, going from the release of the first partial wave packet around $t = -8.8$ fs to time $t = 150$ fs, which is sufficiently long after the interaction for the coordinate-space density to evolve into the shape of the PMD. (d) Comparison of the PMD from the *ab initio* calculation (top frame) with the PMDs from the two-state model (bottom left frame) and the refined five-state model (bottom right frame). All PMDs are normalized to 1.

integrated and scaled momentum distribution is plotted as a dashed orange line in frame (vii) (top). The full 2D PMD is shown in the top frame of Fig. 2(d). It consists of two concentric rings representing the slow and fast components of the AT doublet. The angular distribution exhibits six lobes, i.e., f -type symmetry, as expected for three-photon ionization. The top and bottom lobes of the fast AT component display an additional structure resulting from the interference of the f -type wave packet with a wave packet of p symmetry. The emergence of a p -type wave packet is in accordance with the selection rules and our discussion of ionization pathways in Sec. II B [see also Fig. 1(c)] and consistent with the population of the $3s$ and $4d$ states in Fig. 2(a). Interestingly, the p -type contribution is observed mainly in the fast AT component. In addition, the fast component is enhanced relative to the slow one.

To rationalize these observations we make use of the five-state model, which provides more detailed insights into the role of the individual MPI pathways. The 2D PMD derived from the five-state simulation is shown in the bottom right frame of Fig. 2(d). By fine-tuning the complex-valued ionization amplitudes $a_{n,\ell}$ for the bound-free transitions [58], we obtain excellent agreement with the full 2D-TDSE calculation. The values of the ionization amplitudes used in the simulation are given in Table II. The amplitudes for single-photon ionization from the $3d$ state to either the p - or the f -type continuum and from the $4d$ state to the p -type

continuum are very small. The corresponding photoelectron contributions have no significant influence on the shape of the PMD. One major contribution is due to two-photon ionization from the $2p$ state to both continua. The corresponding 2D PMD is very similar to that obtained with the two-state model, which is shown in the bottom left frame of Fig. 2(d) for comparison, exhibiting a more symmetric AT doublet. The second major contribution is due to single-photon ionization from the $3s$ state to the p -type continuum and from the $4d$ state to the f -type continuum. The corresponding 2D PMD (not

TABLE II. Ionization amplitudes $a_{n,\ell} = |a_{n,\ell}|e^{i\alpha_{n,\ell}}$ used in the five-state model for the transition from the excited bound states to the f -type ($\ell = 3$) and p -type ($\ell = 1$) continua. Single (double) arrows indicate one-photon (two-photon) ionization, treated by first-order (second-order) perturbation theory.

Transition	$ a_{n,\ell} $	$\alpha_{n,\ell}$ (π)
$2p \rightarrow \varepsilon f$	1.00	0.00
$2p \rightarrow \varepsilon p$	0.72	0.49
$3d \rightarrow \varepsilon f$	0.03	0.94
$3d \rightarrow \varepsilon p$	0.10	0.56
$3s \rightarrow \varepsilon p$	0.23	1.30
$4d \rightarrow \varepsilon f$	0.24	0.86
$4d \rightarrow \varepsilon p$	0.01	0.00

shown) exhibits a single ring which, due to the blue detuning of the intermediate states relative to the second-order laser spectrum, overlaps energetically with the fast AT component. Its angular distribution exhibits interference structures in the top and bottom lobes which strongly resemble those observed in the 2D PMD of the full calculation. Hence, ionization from the blue-detuned intermediate states $3s$ and $4d$ is responsible for both the enhancement and the angular structure of the fast AT component.

B. Phase control of the AT doublet via SPODS

Next, we use the *ab initio* ansatz to investigate the control of the AT doublet using shaped pulses, as initially reported in [5,27]. Specifically, we apply double-pulse sequences and use the relative optical phase between the two subpulses to manipulate the contrast of the AT components. The underlying control mechanism was discussed in [3,27] in a dressed-state picture considering a resonantly driven two-state model coupled to the continuum. It was shown that the two AT components map the energy and population of the dressed states of the strongly driven two-state system [28]. The selective emission of a single AT component in the continuum is therefore achieved by the implementation of SPODS in the bound system, in this case via photon locking (PL) [61,62]. PL is based on the initial preparation of a coherent charge oscillation by a resonant prepulse of pulse area $\theta_p = \pi/2$, followed by the phase-sensitive interaction of the induced electric dipole with an intense main pulse. In-phase (antiphase) oscillation of the dipole and field minimizes (maximizes) the interaction energy, which is equivalent to the selective population of the lower (upper) dressed state and, eventually, entails the selective emission of slow (fast) AT electrons. We apply the 2D-TDSE model to assess the validity of this spatiotemporal picture, developed in [31] for the two-state model, on the basis of a more realistic atomic system. For this purpose, we use a sequence of two resonant pulses, a $\pi/2$ prepulse and an intense main pulse of pulse area $\theta_m = 5\pi$, separated in time by $\tau = \tau_2 - \tau_1 = 60$ fs. The field $\mathcal{E}^+(t)$ is shown in Fig. 3(a), decomposed into its envelope (red solid line) and phase. Three different phase settings are depicted. As a reference, the black dotted line indicates the zero relative phase, i.e., both subpulses are in phase ($\Delta\varphi = \varphi_2 - \varphi_1 = 0$). The corresponding 2D PED $\mathcal{P}(\varepsilon, \phi)$ is shown in Fig. 3(c). The PED is very similar to that created by the single pulse in Fig. 2. In particular, both AT components are observed in the spectrum with an asymmetry in favor of the fast AT component, the origin of which was discussed in Sec. III A. Note that, despite the Ramsey-type double-pulse ionization, no interference fringes are observed in the energy spectrum (radial direction), unlike the free-electron wave packets reported in [5,63]. The absence of fringes in the PMD is explained by the different intensities of the two subpulses. The weak prepulse, while preparing the coherence in the bound system, induces only negligible ionization. The major part of the photoelectrons is created by the intense main pulse mapping the bound-state dynamics into the ionization continuum. In contrast to Fig. 3(c), the PED shown in Fig. 3(d) obtained for a relative phase of $\Delta\varphi = \pi/2$ between the main pulse and prepulse [turquoise dashed line in Fig. 3(a)] displays only the fast AT component, while the

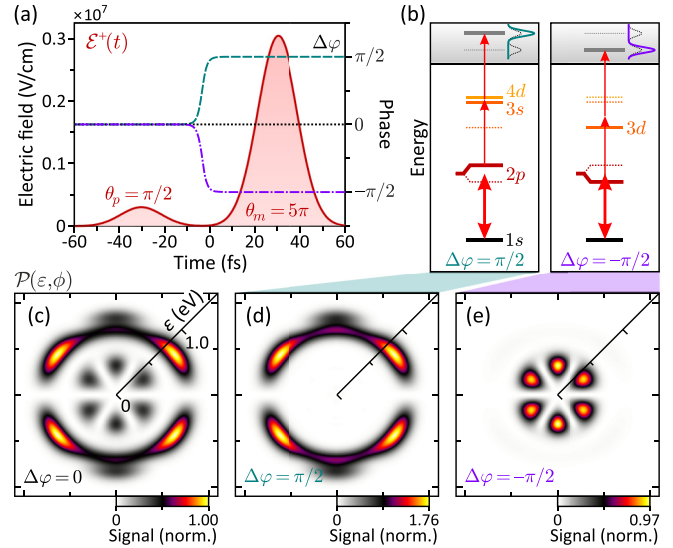


FIG. 3. Switching between the AT components by the relative phase $\Delta\varphi$ of the double-pulse sequence. (a) Electric field $\mathcal{E}^+(t)$ decomposed into amplitude and phase for $\Delta\varphi = 0$ (black dotted line) and $\Delta\varphi = \pm\pi/2$ (turquoise dashed and violet dash-dotted lines). (b) Schematic of the physical mechanism for the selective emission of fast (left frame) and slow (right frame) AT electrons based on SPODS in the resonant $1s$ - $2p$ subsystem. (c) Calculated PED for $\Delta\varphi = 0$ where both AT components are observed. (d) and (e) For $\Delta\varphi = \pm\pi/2$, the photoelectrons switch selectively to the fast and slow AT components, respectively. The three PEDs are normalized to the maximum of the PED in (c).

slow AT electrons are completely suppressed. The amplitude of the fast component has increased by a factor of about 2 compared to that in Fig. 3(c). Setting the relative phase to $\Delta\varphi = -\pi/2$ [violet dash-dotted line in Fig. 3(a)] switches the emitted photoelectrons selectively to the slow AT component at the expense of the fast electrons, as shown in Fig. 3(e). Relative to the PED in Fig. 3(c), the amplitude of the slow component has likewise increased by a factor of 2.

To uncover the dynamics behind the calculated PEDs, we evaluate the time-dependent expectation values of the relevant observables using the wave function. The results are then reproduced by the tailored multistate model to gain access to a dressed-state analysis which eventually reveals the underlying control mechanism. The *ab initio* results are presented in Fig. 4 and compared to the five-state simulation results in Fig. 5. Starting with Fig. 4, the top row shows the dynamics for $\Delta\varphi = \pi/2$ and the selective emission of fast AT electrons [see Fig. 3(d)]. Figure 3(a) shows the population dynamics $\langle p_n \rangle(t)$ of the five relevant atomic states identified in Sec. III A. The $\pi/2$ prepulse excites an electronic wave packet of states $1s$ and $2p$ with equal amplitude. The corresponding charge dynamics is captured by the induced dipole moment $\langle \mu_y \rangle(t)$ shown by the blue line in Fig. 4(b). During the prepulse, the dipole amplitude gradually builds up, oscillating at the Bohr frequency $\omega_{1s,2p} = 2.45$ rad/fs. Closer inspection reveals [see inset (i)] that the dipole follows the driving field with a phase shift of $-\pi/2$, in analogy to a classical oscillator driven on resonance. In this phase configuration, the interaction energy $\langle \varepsilon_{\text{int}} \rangle(t)$, shown by the green line in

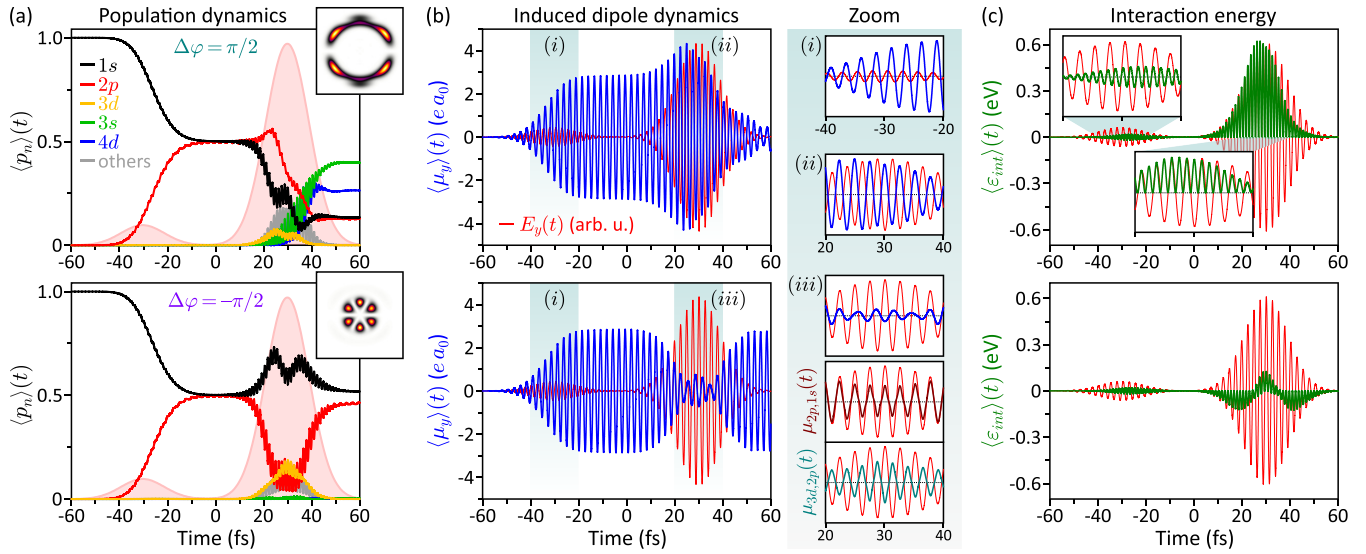


FIG. 4. Evaluation of observables for the selective emission of fast (top row) and slow (bottom row) AT electrons. (a) Population dynamics $\langle p_n \rangle(t)$ induced by the double-pulse sequences. Besides the resonantly coupled states $1s$ and $2p$, the three high-lying intermediate states $3d$, $3s$, and $4d$ are significantly populated. (b) Induced charge dynamics described by the oscillating dipole moment $\langle \mu_y \rangle(t)$ (blue line). The dipole oscillation is compared to the optical oscillation of the driving field $E_y(t)$ (red line). The phase relation between the driving field and induced dipole dynamics determines the interaction energy $\langle \varepsilon_{int} \rangle(t)$, which is evaluated in (c) (green line).

Fig. 4(c), oscillates rapidly around zero (see inset) and hence vanishes on the time average. In the two-state model, this is the signature for the equal population of dressed states [30], associated with no selectivity among the AT components. To verify the relation between the interaction energy and the dressed states, we reproduce the bare-state population dynamics in Fig. 4(a) using the tailored five-state model. The result is shown in the top frame of Fig. 5(a), agreeing very well with the *ab initio* calculation. The derived dressed-state population dynamics, shown in the bottom frame, confirms that during the prepulse, the dressed states of the resonant $1s$ - $2p$ subsystem (black and red lines) are populated equally by 50%. However, this changes drastically during the main pulse. Owing to the $\pi/2$ shift of the optical phase, the field of the main pulse oscillates in antiphase to the induced dipole, as clearly seen in inset (ii) in Fig. 4(b). In this phase configuration, the interaction energy is strictly positive (in fact, maximized), indicating the selective population of the *upper* dressed state in the two-state model [30] associated with the selective emission of fast AT electrons. Again, this is confirmed by the five-state simulation in Fig. 5(a), where we observe the selective population of the upper dressed state of the resonant subsystem (red line) around $t = 0$ with the onset of the main pulse. The bare-state population dynamics induced by the intense main pulse are remarkably different from those induced by the single pulse in Fig. 2(a). Instead of Rabi cycling between the resonantly coupled states $1s$ and $2p$, we observe the synchronous depletion of both states. This is characteristic for PL in a multistate system [8,30]. The population flows from the resonant subsystem selectively to the blue-detuned intermediate states $3s$ and $4d$. To understand this dynamics, we examine the time evolution of the dressed-state energies depicted in Fig. 5(b) [32,35,64]. Around $t = 20$ fs, the upper dressed state approaches the energies of the $3s$ and $4d$ states. Several avoided crossings with the corresponding

dressed states (green and blue lines, respectively) arise, which are relatively narrow due to the weak coupling between the $3s$ and $4d$ states and the resonant $2p$ state (see Table I). As a result, population is transferred nonadiabatically to the blue-detuned intermediate states and further to the fast AT component in the continuum. In the PL scenario, the population is steered selectively along the upper energy channel, whereas in the Rabi scenario some population is stored in the lower dressed state of the resonant subsystem. Therefore, the population transfer to $3s$ and $4d$ is more efficient in the PL scenario, reaching 40% and 26%, respectively [see Fig. 4(a)]. For the same reason, the ionization probability of the fast AT component is enhanced, which explains the increased photoelectron amplitude in Fig. 3(d) relative to Fig. 3(c).

Overall, the results from the 2D-TDSE calculation for the selective emission of fast AT electrons are consistent with those from the two-state model [30,31] and even more so with the multistate models [8] discussed in our earlier work. The reason for the good agreement is the weak coupling of the transit states $3s$ and $4d$ to the resonant state $2p$, due to which these states participate almost perturbatively in the interaction. The energies of the corresponding dressed states are not modified significantly, such that—as the upper dressed state shifts into resonance—the $3s$ and $4d$ dressed states act as mediators to resonantly enhance the otherwise nonresonant two-photon transition from the $2p$ state to the ionization continuum.

In contrast, the selective emission of slow AT electrons observed for $\Delta\varphi = -\pi/2$ [see Fig. 3(e)] evolves via the red-detuned intermediate state $3d$. The coupling of this state to the resonant $2p$ state is stronger than the $1s$ - $2p$ coupling (see Table I). As a result, the dynamics induced by the main pulse is very different in this case, as displayed in the bottom row of Fig. 4. The bare-state population dynamics in Fig. 4(a) is again relatively slow compared to the Rabi scenario in Fig. 2(a). The $1s$ population does not vary significantly, reminiscent of

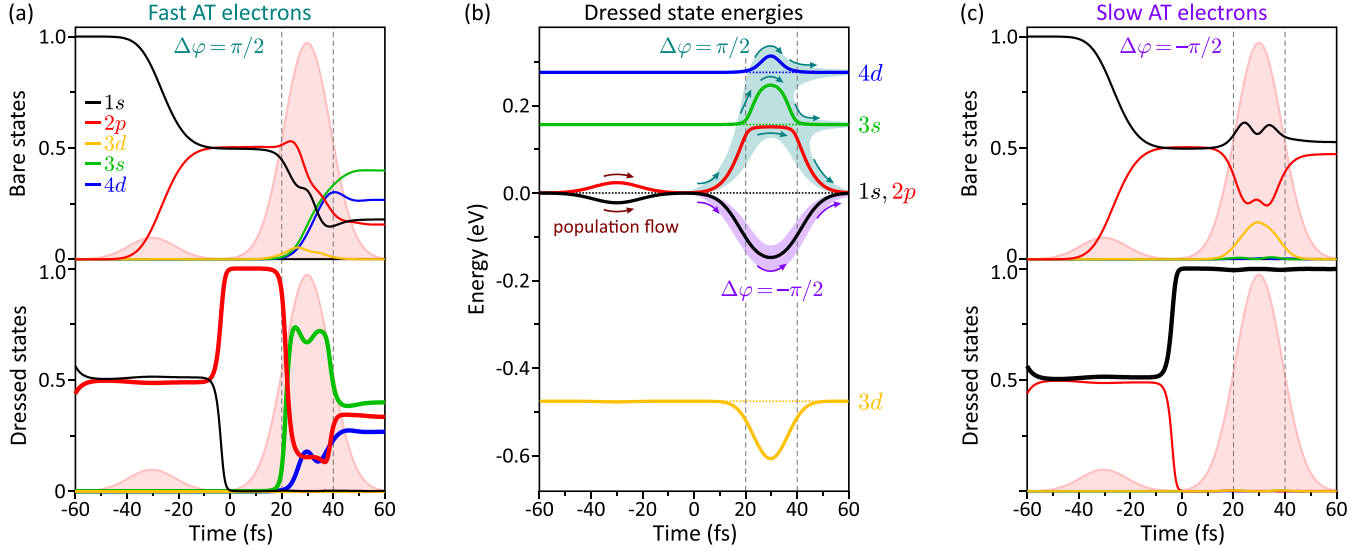


FIG. 5. Dressed-state analysis of the five-state model, performed in a quantum-mechanical frame rotating with the laser central frequency and applying the rotating-wave approximation (for details see, e.g., [30]). The bare-state population dynamics obtained for $\Delta\varphi = \pi/2$ is shown in the top frame of (a). The bottom frame shows the population dynamics of the corresponding dressed states. The time-dependent dressed-state energies, in the chosen quantum-mechanical frame, are shown in (b). The bare-state eigenenergies are depicted as thin dotted horizontal lines. The population flow observed in (a) is indicated by the turquoise shaded area. The selective increase of the interaction energy is responsible for the selective emission of fast AT electrons in the 2D-TDSE model. For $\Delta\varphi = -\pi/2$, the population flow is switched to the lower dressed state of the resonant $1s$ - $2p$ subsystem (black line) by the main pulse, as shown in (c) and indicated by the violet shaded area in (b). This rationalizes the selective emission of slow AT electrons in the 2D-TDSE model.

PL in a two-state system [5,65]. The $2p$ population, however, is depleted during the most intense part of the main pulse. Its population is transferred transiently to the red-detuned $3d$ state while the blue-detuned states, $3s$ and $4d$, receive no population at all. By the end of the interaction, the $3d$ state and all other intermediates are again depopulated, and the $2p$ population is restored, indicating strongly nonresonant excitation conditions. The bare-state population dynamics obtained with the five-state simulation is shown in Fig. 5(c) (top frame), reproducing the main features of the *ab initio* calculation very well.

Due to the $\Delta\varphi = -\pi/2$ phase shift, one would expect the main pulse to oscillate in phase with the dipole induced by the prepulse. However, this is only the case in the leading and trailing edges of the main pulse, as shown in Fig. 4(b) [see the top frame of inset (iii)]. In these time windows, the interaction energy in Fig. 4(c) is strictly negative (minimized), associated with the selective population of the *lower* dressed state in the two-state model. However, during the most intense part of the main pulse, we observe a strong suppression of the dipole amplitude with no well-defined phase relation between the dipole and field [see the top frame of inset (iii)]. This behavior is the result of the competition between two dipoles excited in different subsystems of the atom. One dipole is associated with the $1s$ - $2p$ wave packet excited by the prepulse; the second dipole is associated with the $2p$ - $3d$ wave packet transiently excited by the main pulse. The first dipole is expected to be in phase with the main pulse since both the dipole and the main pulse are phase shifted by $-\pi/2$ relative to the prepulse. The second dipole oscillates in antiphase with the main pulse due to the strongly red detuned excitation. Therefore, both dipoles interfere destructively, which explains

the suppressed amplitude of the total dipole oscillation. To verify this analysis, we calculated the time evolution of the two partial dipole moments

$$\mu_{nm}(t) = \Re[\langle \psi_n | \mu_y | \psi_m \rangle c_n^*(t) c_m(t)] \quad (9)$$

using the state amplitudes $c_n(t) = \langle \psi_n | \psi(t) \rangle$ from the population dynamics in Fig. 4(a). The results are plotted in the middle and bottom frames of inset (iii) by a dark red line for the $\mu_{2p,1s}(t)$ dipole and a turquoise line for the $\mu_{3d,2p}(t)$ dipole. Qualitatively, both curves can be deduced by inspection of the transient population dynamics in Fig. 4(a). In particular, between $t = 20$ and 30 fs we see how the amplitude of the $1s$ - $2p$ dipole decreases due to the depletion of the $2p$ state, while the amplitude of the $2p$ - $3d$ dipole builds up with the population of the $3d$ state. During the central part of the main pulse, the latter even exceeds the former, which explains the sign change in the interaction energy around $t = 30$ fs. Referencing both partial dipoles to the laser field shows that the $1s$ - $2p$ dipole oscillates in phase, while the $2p$ - $3d$ dipole oscillates in antiphase with the main pulse, confirming the above discussion.

In this case, the analysis of the charge dynamics and the interaction energy does not provide a clear physical picture to explain the selective emission of slow AT electrons. In contrast, interpreting the interaction dynamics in the dressed-state picture remains rather transparent. According to the dressed-state population dynamics in Fig. 5(c) (bottom frame) derived from the five-state simulation, the main pulse switches the population around $t = 0$ selectively into the lower dressed state of the resonant subsystem (black line). Following the energy of the lower dressed state in Fig. 5(b), the system

subsequently approaches the red-detuned $3d$ state (yellow line). Due to the larger two-photon detuning of the $3d$ state, on the one hand, and the strong repulsion between the $2p$ and $3d$ dressed states (induced by the strong $3d$ - $2p$ coupling) the system passes the avoided crossing adiabatically, and no population escapes to the $3d$ dressed state. This confirms the nonresonant interaction conditions mentioned above and maintains the selective population of the lower dressed state throughout the main pulse. The nonresonant two-photon ionization from the lower dressed state then explains the selective emission of slow AT electrons.

Based on the above findings we conclude that, in a strongly coupled atomic system, inferring the outcome of the interaction from an analysis of the induced charge dynamics and the interaction energy alone is no longer sufficient. Analyzing the interaction in the dressed-state basis of a specifically adapted and validated multistate model system, however, still provides a clear physical picture of the dynamics, elucidating the role of intermediate states and the structure of the created PMD.

IV. CONCLUSION

In this paper, we applied a numerical model based on the *ab initio* solution of the two-dimensional time-dependent Schrödinger equation to study the nonperturbative phase-control of the Autler-Townes doublet in the photoelectron momentum distribution from $(1+2)$ resonance-enhanced multiphoton ionization of potassium atoms with intense shaped femtosecond laser pulses. We studied the formation dynamics of the AT doublet in the coordinate-space wave function analogously to the spatiotemporal description of above-threshold ionization. Using phase-locked double-pulse sequences, the 2D-TDSE model reproduced the efficient switching between the AT components by the relative optical

phase as demonstrated in previous experiments [3,5,27,28]. So far, the underlying control mechanism has been described by the selective population of dressed states in a two-state model system [30]. However, the analysis of the observables derived from the *ab initio* 2D-TDSE calculation, such as the bound-state population and the induced charge dynamics, revealed significant deviations from the SPODS signatures predicted by the simple two-state model. To rationalize our observations, we proposed a tailored five-state model that included all bound states which were significantly populated in the full calculation and accurately reproduced the 2D PMD. Subsequently, the dressed-state analysis of our five-state model revealed the role of the additional intermediate states. We found that the selective emission of fast AT electrons was promoted by the blue-detuned intermediate states $3s$ and $4d$. Due to their perturbative coupling, these states transiently shifted into resonance with the upper dressed state of the strongly driven $1s$ - $2p$ subsystem and enhanced the otherwise nonresonant two-photon ionization from the $2p$ state. In contrast, the selective emission of slow AT electrons involved the red-detuned and nonperturbatively coupled intermediate state $3d$. In this case, we observed the competition between electric dipole oscillations excited in the resonant $1s$ - $2p$ subsystem and the nonresonantly driven $2p$ - $3d$ subsystem. Generally, the careful design of a tailored multistate model validated against the full *ab initio* calculation [44,45] offers a more complete and clear physical picture of strong-field control in multistate quantum systems.

ACKNOWLEDGMENT

Financial support from the Deutsche Forschungsgemeinschaft via the priority program QUTIF (Program No. SPP1840) is gratefully acknowledged.

-
- [1] N. Dudovich, T. Polack, A. Pe'er, and Y. Silberberg, Simple Route to Strong-Field Coherent Control, *Phys. Rev. Lett.* **94**, 083002 (2005).
 - [2] C. Trallero-Herrero, J. L. Cohen, and T. Weinacht, Strong-Field Atomic Phase Matching, *Phys. Rev. Lett.* **96**, 063603 (2006).
 - [3] M. Wollenhaupt, D. Liese, A. Präkelt, C. Sarpe-Tudoran, and T. Baumert, Quantum control by ultrafast dressed states tailoring, *Chem. Phys. Lett.* **419**, 184 (2006).
 - [4] I. R. Sola, B. Y. Chang, J. Santamaria, V. S. Malinovsky, and J. L. Krause, Selective Excitation of Vibrational States by Shaping of Light-Induced Potentials, *Phys. Rev. Lett.* **85**, 4241 (2000).
 - [5] M. Wollenhaupt, A. Assion, O. Bazhan, C. Horn, D. Liese, C. Sarpe-Tudoran, M. Winter, and T. Baumert, Control of interferences in an Autler-Townes doublet: Symmetry of control parameters, *Phys. Rev. A* **68**, 015401 (2003).
 - [6] B. J. Sussman, D. Townsend, M. Y. Ivanov, and A. Stolow, Dynamic Stark control of photochemical processes, *Science* **314**, 278 (2006).
 - [7] M. Wollenhaupt and T. Baumert, Ultrafast strong field quantum control on K_2 dimers, *J. Photochem. Photobiol. A* **180**, 248 (2006).
 - [8] T. Bayer, H. Braun, C. Sarpe, R. Siemering, P. von den Hoff, R. de Vivie-Riedle, T. Baumert, and M. Wollenhaupt, Charge Oscillation Controlled Molecular Excitation, *Phys. Rev. Lett.* **110**, 123003 (2013).
 - [9] M. E. Corrales, J. González-Vázquez, G. Balerdi, I. R. Solá, R. de Nalda, and L. Bañares, Control of ultrafast molecular photodissociation by laser-field-induced potentials, *Nat. Chem.* **6**, 785 (2014).
 - [10] S. H. Autler and C. H. Townes, Stark effect in rapidly varying fields, *Phys. Rev.* **100**, 703 (1955).
 - [11] H. Stuedel, Berechnung der linienform für den dynamischen starkeffekt bei einstrahlung eines optischen resonanzfeldes, *Ann. Phys. (Berlin, Ger.)* **477**, 113 (1969).
 - [12] T. Hänsch, R. Keil, A. Schabert, C. Schmelzer, and P. Toschek, Interaction of laser light waves by dynamic stark splitting, *Z. Phys.* **226**, 293 (1969).
 - [13] B. K. Teo, D. Feldbaum, T. Cubel, J. R. Guest, P. R. Berman, and G. Raithel, Autler-Townes spectroscopy of the $5S_{1/2}$ - $5P_{3/2}$ - $4d$ cascade of cold ^{85}Rb atoms, *Phys. Rev. A* **68**, 053407 (2003).
 - [14] M. J. Piotrowicz, C. MacCormick, A. Kowalczyk, S. Bergamini, I. I. Beterov, and E. A. Yakshina, Measurement of the electric

- dipole moments for transitions to rubidium Rydberg states via Autler-Townes splitting, *New J. Phys.* **13**, 093012 (2011).
- [15] G. Bevilacqua and E. Arimondo, Bright and dark Autler-Townes states in the atomic Rydberg multilevel spectroscopy, *J. Phys. B* **55**, 154001 (2022).
- [16] S. E. Harris, J. E. Field, and A. Imamoglu, Nonlinear optical Processes Using Electromagnetically Induced Transparency, *Phys. Rev. Lett.* **64**, 1107 (1990).
- [17] M. Fleischhauer, A. Imamoglu, and J. P. Marangos, Electromagnetically induced transparency: Optics in coherent media, *Rev. Mod. Phys.* **77**, 633 (2005).
- [18] J. Dalibard and C. Cohen-Tannoudji, Laser cooling below the Doppler limit by polarization gradients: Simple theoretical models, *J. Opt. Soc. Am. B* **6**, 2023 (1989).
- [19] X. Xu, B. Sun, P. R. Berman, D. G. Steel, A. S. Bracker, D. Gammon, and L. J. Sham, Coherent optical spectroscopy of a strongly driven quantum dot, *Science* **317**, 929 (2007).
- [20] Y. Zhou, A. Rasmita, K. Li, Q. Xiong, I. Aharonovich, and W. Gao, Coherent control of a strongly driven silicon vacancy optical transition in diamond, *Nat. Commun.* **8**, 14451 (2017).
- [21] L. Dusanowski, C. Gustin, S. Hughes, C. Schneider, and S. Höfling, All-optical tuning of indistinguishable single photons generated in three-level quantum systems, *Nano Lett.* **22**, 3562 (2022).
- [22] S. Nandi *et al.*, Observation of Rabi dynamics with a short-wavelength free-electron laser, *Nature (London)* **608**, 488 (2022).
- [23] M. Chini, X. Wang, Y. Cheng, Y. Wu, D. Zhao, D. A. Telnov, S.-I. Chu, and Z. Chang, Sub-cycle oscillations in virtual states brought to light, *Sci. Rep.* **3**, 1105 (2013).
- [24] C. Ott, A. Kaldun, L. Argenti, P. Raith, K. Meyer, M. Laux, Y. Zhang, A. Blättermann, S. Hagstotz, T. Ding, R. Heck, J. Madroñero, F. Martín, and T. Pfeifer, Reconstruction and control of a time-dependent two-electron wave packet, *Nature (London)* **516**, 374 (2014).
- [25] Y. Kobayashi, H. Timmers, M. Sabbar, S. R. Leone, and D. M. Neumark, Attosecond transient-absorption dynamics of xenon core-excited states in a strong driving field, *Phys. Rev. A* **95**, 031401(R) (2017).
- [26] X. Wu, Z. Yang, S. Zhang, X. Ma, J. Liu, and D. Ye, Buildup time of Autler-Townes splitting in attosecond transient absorption spectroscopy, *Phys. Rev. A* **103**, L061102 (2021).
- [27] M. Wollenhaupt, A. Präkelt, C. Sarpe-Tudoran, D. Liese, and T. Baumert, Strong field quantum control by selective population of dressed states, *J. Opt. B* **7**, S270 (2005).
- [28] M. Wollenhaupt, A. Präkelt, C. Sarpe-Tudoran, D. Liese, T. Bayer, and T. Baumert, Femtosecond strong-field quantum control with sinusoidally phase-modulated pulses, *Phys. Rev. A* **73**, 063409 (2006).
- [29] M. Wollenhaupt, A. Präkelt, C. Sarpe-Tudoran, D. Liese, and T. Baumert, Quantum control by selective population of dressed states using intense chirped femtosecond laser pulses, *Appl. Phys. B* **82**, 183 (2006).
- [30] T. Bayer, M. Wollenhaupt, H. Braun, and T. Baumert, Ultrafast and efficient control of coherent electron dynamics via SPODS, *Adv. Chem. Phys.* **159**, 235 (2016).
- [31] T. Bayer, M. Wollenhaupt, and T. Baumert, Strong-field control landscapes of coherent electronic excitation, *J. Phys. B* **41**, 074007 (2008).
- [32] N. V. Vitanov, T. Halfmann, B. W. Shore, and K. Bergmann, Laser-induced population transfer by adiabatic passage techniques, *Annu. Rev. Phys. Chem.* **52**, 763 (2001).
- [33] B. W. Shore, *Manipulating Quantum Structures Using Laser Pulses* (Cambridge University Press, Cambridge, 2011).
- [34] C. Meier and V. Engel, Interference Structure in the Photoelectron Spectra Obtained from Multiphoton Ionization of Na₂ with a Strong Femtosecond Laser Pulse, *Phys. Rev. Lett.* **73**, 3207 (1994).
- [35] M. Krug, T. Bayer, M. Wollenhaupt, C. Sarpe-Tudoran, T. Baumert, S. S. Ivanov, and N. V. Vitanov, Coherent strong-field control of multiple states by a single chirped femtosecond laser pulse, *New J. Phys.* **11**, 105051 (2009).
- [36] K. Eickhoff, S. Kerbstadt, T. Bayer, and M. Wollenhaupt, Dynamic quantum state holography, *Phys. Rev. A* **101**, 013430 (2020).
- [37] T. Bayer, C. Philipp, K. Eickhoff, and M. Wollenhaupt, Atomic photoionization dynamics in ultrashort cycloidal laser fields, *Phys. Rev. A* **102**, 013104 (2020).
- [38] D. Pengel, S. Kerbstadt, L. Englert, T. Bayer, and M. Wollenhaupt, Control of three-dimensional electron vortices from femtosecond multiphoton ionization, *Phys. Rev. A* **96**, 043426 (2017).
- [39] S. Kerbstadt, K. Eickhoff, T. Bayer, and M. Wollenhaupt, Odd electron wave packets from cycloidal ultrashort laser fields, *Nat. Commun.* **10**, 658 (2019).
- [40] J. M. Ngoko Djiokap, S. X. Hu, L. B. Madsen, N. L. Manakov, A. V. Meremianin, and A. F. Starace, Electron Vortices in Photoionization by Circularly Polarized Attosecond Pulses, *Phys. Rev. Lett.* **115**, 113004 (2015).
- [41] T. Bayer and M. Wollenhaupt, Molecular free electron vortices in photoionization by polarization-tailored ultrashort laser pulses, *Front. Chem.* **10**, 899461 (2022).
- [42] K.-J. Yuan, S. Chelkowski, and A. D. Bandrauk, Photoelectron momentum distributions of molecules in bichromatic circularly polarized attosecond UV laser fields, *Phys. Rev. A* **93**, 053425 (2016).
- [43] T. Bayer, M. Wollenhaupt, C. Sarpe-Tudoran, and T. Baumert, Robust Photon Locking, *Phys. Rev. Lett.* **102**, 023004 (2009).
- [44] D. Younis and J. H. Eberly, Benchmark of few-level quantum theory vs *ab initio* numerical solutions for the strong-field Autler-Townes effect in photoionization of hydrogen, *J. Phys. B* **55**, 164001 (2022).
- [45] A. Tóth, S. Borbély, Y. Zhou, and A. Csehi, Role of dynamic stark shifts in strong-field excitation and subsequent ionization, *Phys. Rev. A* **107**, 053101 (2023).
- [46] D. Bauer, *Computational Strong-Field Quantum Dynamics. Intense Light-Matter Interactions* (De Gruyter, Berlin, 2017), Vol. 1.
- [47] M. Sprik and M. L. Klein, Optimization of a distributed Gaussian basis set using simulated annealing: Application to the adiabatic dynamics of the solvated electron, *J. Chem. Phys.* **89**, 1592 (1988).
- [48] S. Shin and H. Metiu, Nonadiabatic effects on the charge transfer rate constant: A numerical study of a simple model system, *J. Chem. Phys.* **102**, 9285 (1995).
- [49] M. Erdmann, E. K. U. Gross, and V. Engel, Time-dependent electron localization functions for coupled nuclear-electronic motion, *J. Chem. Phys.* **121**, 9666 (2004).

- [50] C. C. Marston and G. G. Balint-Kurti, The Fourier grid Hamiltonian method for bound state eigenvalues and eigenfunctions, *J. Chem. Phys.* **91**, 3571 (1989).
- [51] A. Kramida, Y. Rachenko, and J. Reader, NIST Atomic Spectra Database, <https://www.nist.gov/pml/atomic-spectra-database>.
- [52] R. Kosloff and H. Tal-Ezer, A direct relaxation method for calculating eigenfunctions and eigenvalues of the Schrodinger equation, *Chem. Phys. Lett.* **127**, 223 (1986).
- [53] M. D. Feit, J. A. Fleck, and A. Steiger, Solution of the Schrödinger equation by a spectral method, *J. Comput. Phys.* **47**, 412 (1982).
- [54] R. Kosloff and D. Kosloff, Absorbing boundaries for wave propagation problems, *J. Comput. Phys.* **63**, 363 (1986).
- [55] R. Santra, Why complex absorbing potentials work: A discrete-variable-representation perspective, *Phys. Rev. A* **74**, 034701 (2006).
- [56] R. Heather and H. Metiu, An efficient procedure for calculating the evolution of the wave function by fast Fourier transform methods for systems with spatially extended wave function and localized potential, *J. Chem. Phys.* **86**, 5009 (1987).
- [57] M. Winter, M. Wollenhaupt, and T. Baumert, Coherent matter waves for ultrafast laser pulse characterization, *Opt. Commun.* **264**, 285 (2006).
- [58] P. Hockett, M. Wollenhaupt, C. Lux, and T. Baumert, Complete Photoionization Experiments via Ultrafast Coherent Control with Polarization Multiplexing, *Phys. Rev. Lett.* **112**, 223001 (2014).
- [59] G. Mainfray and C. Manus, Multiphoton ionization of atoms, *Rep. Prog. Phys.* **54**, 1333 (1991).
- [60] P. Agostini, F. Fabre, G. Mainfray, G. Petite, and N. K. Rahman, Free-Free Transitions Following Six-Photon Ionization of Xenon Atoms, *Phys. Rev. Lett.* **42**, 1127 (1979).
- [61] E. T. Sleva, I. M. Xavier, Jr., and A. H. Zewail, Photon locking, *J. Opt. Soc. Am. B* **3**, 483 (1986).
- [62] Y. S. Bai, A. G. Yodh, and T. W. Mossberg, Selective Excitation of Dressed Atomic States by Use of Phase-Controlled Optical Fields, *Phys. Rev. Lett.* **55**, 1277 (1985).
- [63] M. Wollenhaupt, A. Assion, D. Liese, C. Sarpe-Tudoran, T. Baumert, S. Zamith, M. A. Bouchene, B. Girard, A. Flettner, U. Weichmann, and G. Gerber, Interferences of Ultrashort Free Electron Wave Packets, *Phys. Rev. Lett.* **89**, 173001 (2002).
- [64] M. Wollenhaupt, T. Bayer, N. V. Vitanov, and T. Baumert, Three-state selective population of dressed states via generalized spectral phase-step modulation, *Phys. Rev. A* **81**, 053422 (2010).
- [65] R. Kosloff, A. D. Hammerich, and D. Tannor, Excitation without Demolition: Radiative Excitation of Ground-Surface Vibration by Impulsive Stimulated Raman Scattering with Damage Control, *Phys. Rev. Lett.* **69**, 2172 (1992).